Catalysis Science & Technology

ROYAL SOCIETY OF CHEMISTRY

PAPER

View Article Online
View Journal | View Issue

Cite this: *Catal. Sci. Technol.*, 2021, 11, 6191

Metal free-covalent triazine frameworks as oxygen reduction reaction catalysts – structure–electrochemical activity relationship†

Turgut Sönmez, ‡[ab] Kendra Solveig Belthle,‡[ac] Andree Iemhoff,[a] Jan Uecker,[a] Jens Artz,[a] Timo Bisswanger,[d] Christoph Stampfer,[d] Hairul Hisham Hamzah,[e] Sabina Alexandra Nicolae,[f] Maria-Magdalena Titirici[f] and Regina Palkovits *[a]

Nitrogen-rich porous carbon polymers are highly promising oxygen reduction reaction (ORR) catalysts and possess great potential to replace Pt-based precious metals used in energy storage and conversion systems. In this study, covalent triazine frameworks (CTFs) were synthesized *via* an ionothermal route based on different monomers and synthesis temperatures (400–750 °C) and tested in alkaline media with a rotating disk electrode (RDE). The effect of the applied monomer and temperature on the surface functionalities of the frameworks and thus correlation to their ORR activities are deeply discussed. Micro/mesoporous, hierarchically ordered and highly conductive N-rich materials with up to 2407 $m^2 g^{-1}$ specific surface areas and 2.49 $cm^3 g^{-1}$ pore volumes were achievable. Owing to the high surface area (1742 $m^2 g^{-1}$), pore volume (1.56 $cm^3 g^{-1}$), highest conductivity, electrochemically active surface area and hierarchical mesoporous structure, CTF DCBP-750 facilitated 0.9 V onset potential (only 0.06 V larger than that of the benchmark 10 wt% Pt/C) with 5.1 mA cm^{-2} limiting current density. In addition to the structural properties, graphitic nitrogen species, active sites responsible for binding and activating O_2, rather than pyridinic nitrogen appear to be more important for the overall ORR performance. Thus, the trade-off point is crucial to obtain optimal ORR activity with metal-free CTFs.

Received 7th March 2021,
Accepted 11th June 2021

DOI: 10.1039/d1cy00405k

rsc.li/catalysis

Introduction

Renewable energy technologies such as fuel cells and metal–air batteries have been the centre of tremendous attention for decades as such energy conversion and storage systems provide great potential to fulfil the global energy demands. The commercialization of the aforementioned systems in an industrial scale depends on the performance of the oxygen reduction reaction (ORR), a critical process in such devices. Pt-based precious metals have been known to be the most active ORR catalysts; however, their high cost, scarcity, poor durability and the sluggish electron transfer kinetics still remain big challenges to overcome.[1–5] Therefore, there have been great efforts to replace Pt/Pt alloys with non-precious metal catalysts,[6,7] metal oxides (such as perovskites,[8–10] spinels[11,12]) or metal-free carbon-based materials (N-doped carbon films,[13] N-doped graphene,[14,15] carbon nanosheets,[16] carbon nanotubes[17] *etc.*) for the ORR over the years. Even though various N-containing carbon materials as either catalysts or supports have shown considerably high ORR performances, these materials still remain in an unsatisfactory level. Therefore, there is still a need for designing and developing metal-free materials exhibiting high catalytic activity and durability in the ORR.

Covalent triazine frameworks (CTFs)[18,19] as N-containing porous carbonaceous polymers and a subclass of covalent organic frameworks (COFs)[3,18,20,21] offer a great potential for ORR. They are more advantageous than other carbon-based materials as their structure and N-content and type of N-sites can be tuned precisely by selection of different monomers with varying aromatic structure elements and their synthesis

[a] *Institut für Technische und Makromolekulare Chemie, RWTH Aachen University, Worringerweg 2, 52074 Aachen, Germany. E-mail: palkovits@itmc.rwth-aachen.de*
[b] *Department of Energy Systems Engineering, Technology Faculty, Karabuk University, 78050 Karabük, Turkey*
[c] *Max-Planck-Institut für Kohlenforschung, Kaiser-Wilhelm-Platz 1, Mülheim an der Ruhr, D-45470, Germany*
[d] *JARA-FIT and 2nd Institute of Physics A, RWTH Aachen University, 52074 Aachen, Germany*
[e] *School of Chemical Sciences, Universiti Sains Malaysia (USM), 11800, Gelugor, Penang, Malaysia*
[f] *School of Engineering and Materials Science and Materials Research Institute, Queen Mary University of London, London E14 NS, UK*
† Electronic supplementary information (ESI) available. See DOI: 10.1039/d1cy00405k
‡ These authors contributed equally to this work.

temperature. Besides adjustable physical and chemical properties, CTF materials are highly robust, chemically and thermally stable (up to 400 °C) under either strong acidic or basic conditions, making them promising candidates for a variety of applications.[18,22,23] Important parameters such as porosity, pore size distribution, specific surface area, surface polarity, nitrogen content *etc.* can be adjusted to the desired surface functionalities.[18,24] Kuhn *et al.* have shown the influence of differing applied monomers and monomer/$ZnCl_2$ ratios on the surface functionalities of the resulting materials. CTFs possessed specific surface areas and pore volumes of up to 2475 $m^2\ g^{-1}$ and 2.44 $cm^3\ g^{-1}$, respectively.[19] In their later study, a change in porosity and chemical composition of the scaffolds (at a loss of nitrogen at elevated temperatures) was observed with increasing reaction temperature, and a CTF with 3300 $m^2\ g^{-1}$ specific surface area and 2.4 $cm^3\ g^{-1}$ pore volume was accessible.[22] The CTF serves either as a catalyst itself or as a support material for binding active metal species due to its N content. In general, nitrogen creates disordered nanocarbon structures and donates electrons to carbon, thereby C–N active sites facilitate the ORR.[6,18,25] In addition to other structural parameters, N content and more importantly N configurations (pyridinic, pyrrolic and graphitic) and their ratios in CTF materials play a crucial role in the overall ORR performance.[1] Therefore, designing and defining the optimal structural properties (surface area, porosity, polarity, hierarchical structure *etc.*) and nitrogen content as well as identifying the active N species (either pyridinic or graphitic) in CTF materials for the ORR are highly desired. There have been various studies[1,3,26] that investigated metal-free CTFs for the ORR; however, to the best of our knowledge, this work is the first study focusing on the dependence of the electrochemical activity on the structure of metal-free CTFs by varying the applied monomers and the synthesis temperature to provide an optimized structure for the ORR in alkaline media.

Herein, CTFs are chosen as catalysts to elucidate the structure–electrochemical activity relationship and contribute to the identification of active species in the ORR for rational catalyst design. The purpose is to distinguish the effect of different parameters such as surface area, porosity, nitrogen content, ratio of different nitrogen configurations, conductivity, degree of graphitization and defects on the ORR performance

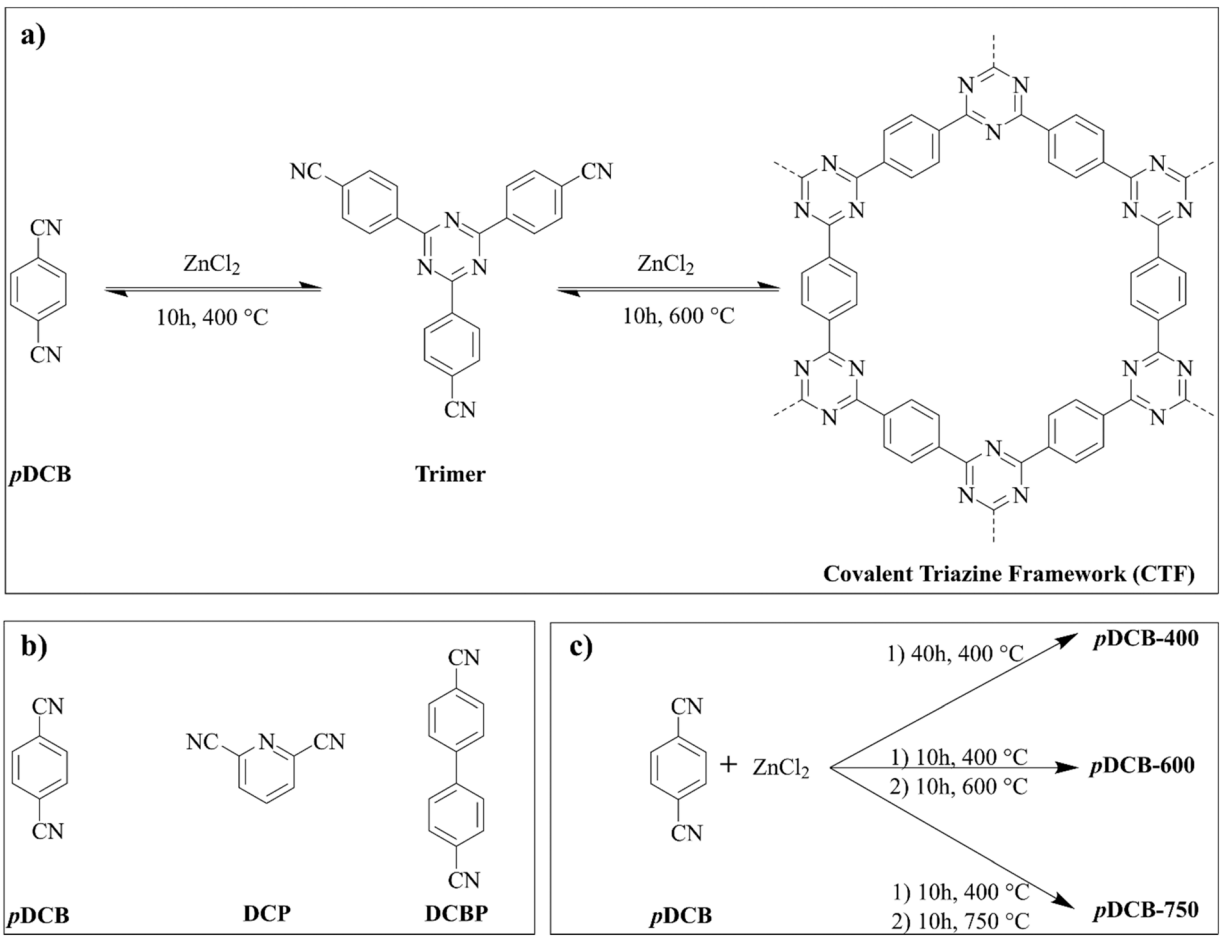

Scheme 1 (a) Idealized ionothermal synthesis of CTF based on the monomer 1,4-dicyanobenzene (*p*DCB) in molten $ZnCl_2$ in two steps. (b) 3M monomer building blocks used in this study. (c) Synthesis of 3T-CTFs based on 1,4-dicyanobenzene (*p*DCB). Ultra dry $ZnCl_2$ was used at 750 °C to prevent bursting.

in alkaline media. To do this, CTFs were firstly synthesized from different monomers (3M-CTF, 2,6-pyridinedicarbonitrile (DCP), 1,4-dicyanobenzene (*p*DCB) and 4,4′-biphenyldicarbonitrile (DCBP)) *via* an ionothermal synthesis[19] and based on the monomer *p*DCB at different synthesis temperatures (3T-CTF, 400, 600 and 750 °C) for the second step of the ionothermal route (Scheme 1). Further electrocatalytic performance optimization was carried out based on the results of different applied monomers and synthesis temperatures. Among the 3M-CTFs, DCBP has shown the most positive onset potential (0.85 V *vs.* RHE) due to its hierarchical mesoporous structure and the largest electrochemical active surface area. The ORR activity was greatly enhanced at elevated synthesis temperatures due to the obvious transition from pyridinic to graphitic nitrogen, increased conductivity, surface area and pore volume, leading to more hierarchical structures, whereas a decrease in nitrogen content occurred. Amongst all CTFs in this study, the most positive onset potential (0.9 V *vs.* RHE) was obtained at optimized DCBP-750 with only 0.06 V larger than that of the benchmark catalyst, 10 wt% Pt/C. In addition to the correlation of various structural parameters to the ORR performance, the study also emphasizes graphitic N as the active site rather than pyridinic N for binding and activating O_2.

Experimental

Materials

2,6-Pyridinedicarbonitrile ($C_7H_3N_3$, 97%, Merck), 1,4-dicyanobenzene ($C_6H_4(CN)_2$, 98%, Merck), 4,4′-biphenyldicarbonitrile ($NCC_6H_4C_6H_4CN$, 97%, Merck), zinc chloride Redi-Dri ($ZnCl_2$, >98%, Sigma-Aldrich), zinc chloride ultra dry ($ZnCl_2$, 99.999%, Sigma-Aldrich), tetrahydrofuran ($(CH_2)_4O$, Chemsolute), hydrochloric acid (HCl_{aq}, ≥37 wt%, Chemsolute), potassium hydroxide (KOH, ≥85%, Chemsolute), sodium hydroxide (NaOH, ≥99.5%, Chemsolute), Nafion® 117 solution (5%, Sigma-Aldrich), Carbon Black Super P® (C, ≥99%, Alfa Aesar), 10 wt% Pt/C (HiSPEC 2000), ethanol absolute (EtOH, ≥99.9%, Chemsolute), oxygen (Westfalen-Gases), nitrogen (Westfalen-Gases) and deionized water. All materials were used as received without further purification.

Synthesis of CTF catalysts

All CTF materials were synthesized *via* an ionothermal route (see Scheme 1a) in quartz glass ampoules following literature procedures.[19,22,27–29] For a common synthesis of a 3M-CTF based on 2,6-pyridinedicarbonitrile (DCP), a mixture of monomer (3 g, 23.4 mmol, 1 eq.) and $ZnCl_2$ (15.96 g, 117.1 mmol, 5 eq.) was ground within a glove box and transferred into a quartz glass ampoule (height: 12 cm, diameter: 3 cm). The ampoule was evacuated and flame-sealed prior to being placed inside a furnace. In the first step, the sample was heated to 400 °C for 10 hours and then to 600 °C in the second step for 10 hours at a heating rate of 10 °C min^{-1}. After cooling to room temperature, the ampoule was opened (**Caution**; the ampoule is under pressure due to high temperature treatment, so the pressure is released during opening) and the black monolith was soaked in HCl (1 M) and stirred for one hour. The monolith was ground and washed with excess deionized (DI) water and HCl (1 M). The solid was ground in a ball mill (Fritsch Pulverisette23, 5 min, 30 Hz) and stirred in aq. HCl (1 M, 400 mL) at room temperature overnight to remove the remaining $ZnCl_2$. The material was washed in sequence with water, HCl (1 M), $NaOH_{aq}$ (1 M), water and tetrahydrofuran (THF), using 250 mL for each step. Finally, the product was dried at 60 °C under vacuum and a black powder in nearly quantitative yield (>95%) was obtained. In the same way, 3M-CTFs *p*DCB and DCBP were synthesized based on their monomers, 1,4-dicyanobenzene and 4,4′-biphenyldicarbonitrile, respectively. The as-synthesized materials are named by the shortcut of the respective monomer unit together with the temperature during the second temperature step (see Scheme 1b and c). For instance, *p*DCB-750 refers to 3T-CTF synthesized from 1,4-dicyanobenzene at 400 °C in the first and 750 °C in the second step. If no temperature is given, the 3M-CTF was synthesized by the standard procedure as described above. When applying synthesis temperatures higher than 600 °C in the second step, ultra-dry $ZnCl_2$ (see Materials section) was used to prevent bursting of the glass ampoule. The heating time in the first step for all CTF materials was 10 hours except for the CTF *p*DCB-400 sample, where 40 hours reaction time was used according to the literature.[19]

Characterization

Elemental analyses were performed on an Elementar (vario EL cube) elemental analyser in CHN operation mode. The instrument was calibrated by blank measurements and using the internal standard acetanilide. The CTFs were combusted and the weight percent of carbon, hydrogen and nitrogen in the combustion products were determined. A Micrometrics ASAP 2000 was used for the nitrogen physisorption measurements. The CTFs were first degassed at 200 °C for 18 hours in a FloVac Degasser. The measurements were performed at liquid nitrogen temperature (−196 °C) by a static volumetric method. The specific surface areas were determined by using the Brunauer–Emmett–Teller (BET) model at relative pressure values between 0.05 and 0.3. Total pore volumes were derived from the adsorption at $p/p_0 = 0.95$ according to Gurvich's rule. The XPS measurements were conducted on a Thermo Fisher Nexsa spectrometer equipped with a 180° hemispherical analyser using Al $K_{\alpha 1}$ (1486.74 eV) radiation produced by a monochromatized X-ray source. The base pressure of the system was *ca.* 1×10^{-8} torr increasing to *ca.* 4×10^{-8} torr during the analysis of these samples. Samples were mounted using conductive carbon tape and the surface was ion etched to ensure the purity of each sample. The deconvolution and data processing was done using the Avantage™ software. Raman spectra were taken with a confocal WITec Alpha300R microscope. The microscope was

equipped with a 532 nm solid-state laser. The obtained Raman intensity data were smoothed using a FFT filter at 10 points before plotting.

Electrochemical measurements and electrode coating

All electrochemical measurements were carried out with an Autolab PGSTAT 302N instrument and the Nova software package. The rotation rates of the respective experiments were controlled by a Metrohm motor controller equipped with a rotating disk electrode (RDE) unit. A typical three-electrode configuration in an electrochemical glass cell (volume ~100 mL) was used for the electrochemical experiments. Glassy carbon, Ag/AgCl (containing 3 M KCl) and platinum were used in an undivided cell as the working, reference, and counter electrode, respectively. All the measured potentials were corrected to the reversible hydrogen electrode (RHE) for a better comparison according to the formula E_{RHE} (V) = $E_{Ag/AgCl}$ + 0.21 + 0.059 × pH. The experiments were performed in 0.1 M KOH (pH ~12.8) at room temperature. Unless otherwise stated, the electrolyte was purged with O_2 for at least 10 minutes as this proved to be sufficient to saturate the solution and it was controlled *via* an IR oxygen sensor prior to each measurement, including the repeated purging of O_2 into the electrolyte between each of the measurements at different rotational speeds. During the measurements, the O_2 inlet was placed above the electrolyte to keep the atmosphere above the electrolyte saturated with O_2.

Thin-film working electrodes were prepared *via* drop casting the catalyst ink onto the glassy carbon (GC) inside the RDE tip (Sigradur G, HTW GmbH, 4 mm diameter, 0.126 cm^2 area). Prior to the drop-casting, the electrode was pretreated by polishing with micro-cloths (Buhler) and Al_2O_3 suspensions with different particle sizes (first 1 μm and then 0.05 μm, Buhler). The tip was sonicated afterwards in a mixture of deionized water and ethanol for 10 minutes to obtain a mirror-clean surface. The catalyst ink was prepared by dispersing 3 mg of the catalyst powder in a 600 μL solution containing 294 μL deionized water, 294 μL ethanol and 12 μL Nafion. The ink was sonicated in an ultrasonic bath (Sonorex Super RK 102 H) for 30 minutes followed by 2 minutes shaking in a vortex (Grant-bio, PV-1) to obtain a homogeneous ink. 1 × 5 μL of ink was applied onto the clean GC disk to obtain a uniform thin-film electrode (0.2 mg cm^{-2} catalyst loading) and then the electrode was dried at atmospheric conditions for at least 20 minutes. The small amount of Nafion in the ink was found to enhance the stability of the thin-film electrode in order to obtain reproducible measurements. For a comparison of the electrochemical activities of all CTF materials, they were benchmarked against Carbon Super P and commercial 10 wt% Pt/C. Additionally; the ORR mechanisms ($4e^-$ or $2e^-$ pathway) of the CTFs were evaluated and compared to what is known for Carbon Super P and 10 wt% Pt/C under the same conditions. Pt exhibits a $4e^-$ reduction of O_2 while graphitic carbon shows a $2e^-$ pathway.[11] Thin-film electrodes of Carbon Super P and 10 wt% Pt/C were prepared using the same procedure as described above. The electrochemical measurements were repeated more than once to prove the reproducibility of the measurements. The Origin software package was used for data processing.

Results and discussion

CTF materials were synthesized from different monomer building blocks (3M) and at different synthesis temperatures (3T) ranging from 400 to 750 °C (see Scheme 1b and c). $ZnCl_2$ was used as solvent during the synthesis, besides serving as a Lewis acid catalyst and a porogen.[30] A monomer : $ZnCl_2$ molar ratio of 1 : 5 was sufficient to synthesize porous CTF materials with high surface areas and was applied in this study.[29,30]

The C, H, and N elemental analysis results of the 3M-CTF materials are shown in Table 1, entries 1–3 (Table S1, ESI,† for full elemental analysis). For all 3M-CTFs, the nitrogen content (N [wt%]) decreased compared to the theoretical nitrogen contents in the applied monomer units (Table S2, ESI†), which is due to side reactions, such as partial carbonization, taking place at elevated temperatures in the presence of $ZnCl_2$.[31] As the pyridinic monomer unit (DCP) contains the highest theoretical nitrogen content compared to other monomers (*p*DCB and DCBP), the nitrogen content in the corresponding framework is the highest (18.8%, Table 1, entry 1). Correspondingly, the molar C/N ratios range from 3.7 in CTF DCP to 18.7 in CTF DCBP. In agreement with literature data, nitrogen contents in the 3T-CTFs based on 1,4-dicyanobenzene

Table 1 Elemental analysis (N [wt%] and C/N molar ratios), nitrogen physisorption, N 1s XPS data of different nitrogen configurations (pyridinic, pyrrolic and graphitic N), and Raman spectroscopy (relative intensities of D- and G-bands) data of CTF materials. Entries 2 and 5 are the same material (for an easier comparison at different *T*)

		Elemental analysis		N_2 physisorption		N 1s XPS			Raman
Entry	CTF	N [wt%]	Molar C/N	S_{BET} [m^2 g^{-1}]	V_p [cm^3 g^{-1}]	N_{pyri} [%]	N_{pyrr} [%]	N_{gra} [%]	I_D/I_G
1	DCP	18.8	3.7	1050	0.57	52.1	26.5	21.4	1.57 ± 0.01
2	*p*DCB	11.4	8.0	2358	2.18	30.3	23.4	46.3	1.40 ± 0.01
3	DCBP	5.3	18.7	2164	1.58	48.6	18.9	32.5	1.21 ± 0.02
4	*p*DCB-400	13.5	6.3	1172	0.66	40.2	28.5	31.3	1.39 ± 0.03
5	*p*DCB-600	11.4	8.0	2358	2.18	30.3	23.4	46.3	1.40 ± 0.01
6	*p*DCB-750	6.3	14.2	2407	2.49	35.2	21.7	43.1	1.25 ± 0.03
7	DCBP-750	3.4	30.3	1742	1.56	39.0	18.9	42.1	1.19 ± 0.04

(*p*DCB) decrease with increasing synthesis temperature (Table 1, entries 4–6).[26] This effect is more pronounced at higher temperatures, where a drastic drop (from 11.4 to 6.3) is observed in the transition from 600 to 750 °C in the second temperature set-point. At these temperatures, irreversible side reactions and subsequent carbonization of the framework become increasingly important reaction pathways, leading to a lower nitrogen content.[28,32]

The nitrogen physisorption measurements of the CTF materials reveal that specific surface areas, based on the Brunauer–Emmett–Teller (BET) model, range from 1050 to above 2400 $m^2\ g^{-1}$ alongside a total pore volume of up to 2.5 $cm^3\ g^{-1}$ (Table 1, entry 6). The corresponding adsorption isotherms for all CTF materials are depicted in Fig. S1 (ESI†). While 3M-CTF DCP presents a type I isotherm characteristic for fully microporous materials, 3M-CTF *p*DCB and DCBP show type IV isotherms with an H2 hysteresis loop located between 0.4 and 0.8 p/p_0, indicating mesoporous structures (Fig. S1a, ESI†).[32] As highlighted in the literature, this difference in porosity can mainly be attributed to a strong interaction between zinc chloride and pyridinic nitrogen moieties of the monomer during polymerization, which causes a more dense coordination geometry during polymerization.[28,32] Consequently, 3M-CTF DCP possesses the smallest surface area (1050 $m^2\ g^{-1}$) and total pore volume (0.57 $cm^3\ g^{-1}$). In contrast, the highest surface areas (2358 $m^2\ g^{-1}$) and total pore volumes (2.18 $cm^3\ g^{-1}$) were obtained when using *p*DCB as monomer (Table 1, entry 2). The structural properties of the CTFs investigated herein are in accordance with previous reports.[30] A comparison of the N_2 physisorption isotherms of the 3T-CTFs based on *p*DCB as monomer and synthesized at varying temperatures reveals the increasing influence of side reactions at elevated temperatures (Table 1, entries 4–6). While a purely microporous material with a type I isotherm is obtained at 400 °C, the shape changes to type IV upon increasing the temperature, indicating the formation of additional mesopores (Fig. S1b, ESI†). Moreover, the specific surface area and total pore volume of the CTFs double during this transition (Table 1, entries 4–5). The increase in porosity is more pronounced between 400 and 600 °C compared to 750 °C, as opposed to the results from elemental analysis.

In CTF materials, different nitrogen species are formed as a result of carbonization.[31] Different studies have proposed the involvement of nitrogen moieties and correlated the electrocatalytic ORR performance of the materials with the ratio of different nitrogen species.[33] There is still controversy about which species is the active site for the ORR and while some studies[34,35] suggest graphitic nitrogen to be the most active, others[13,14,17] point out pyridine-type ones. Therefore, XPS measurements were taken to investigate the chemical composition of all CTFs used in this work (Table S3, ESI†) and to show their nitrogen configurations. XPS N 1s spectra were deconvoluted according to the assignment by a recent study conducted by Cao *et al.*,[3] and all CTFs show three different types of nitrogen configurations located at 398.3 ± 0.3, 399.4 ± 0.3 and 400.7 ± 0.2 eV corresponding to pyridinic (N_{pyri}), pyrrolic (N_{pyrr}), and graphitic nitrogen (N_{gra}), respectively (Fig. 1). The share of a certain nitrogen species is derived from the areas of

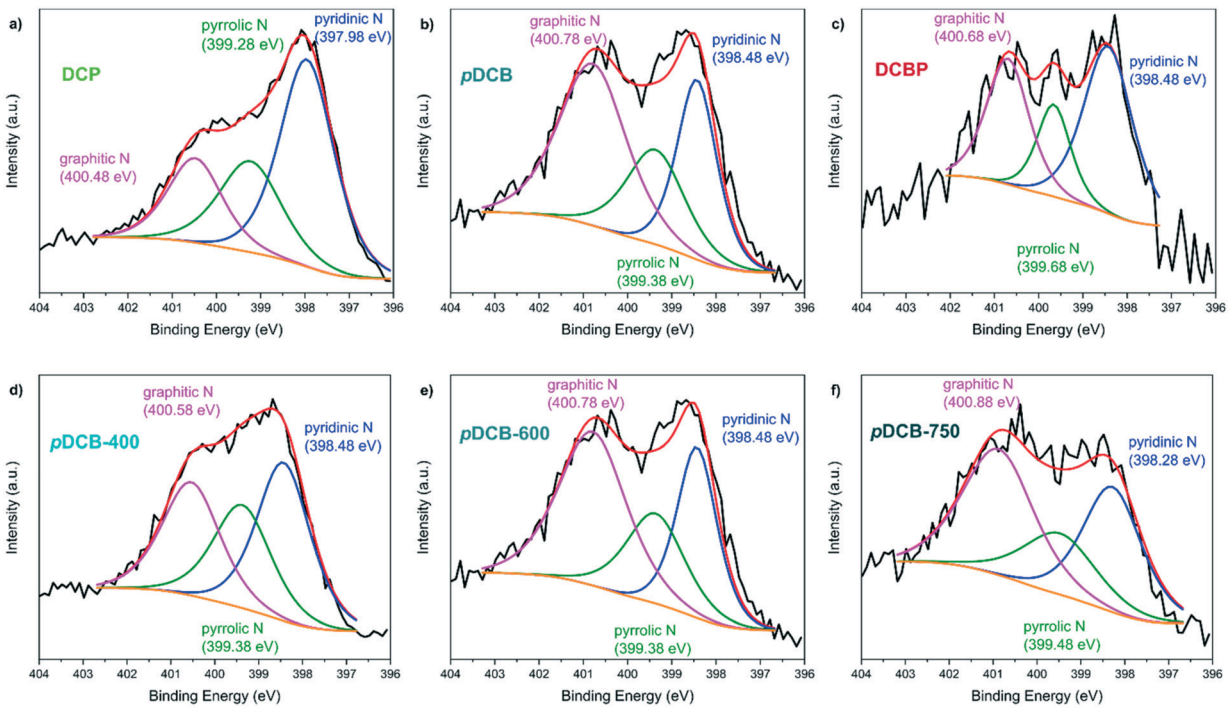

Fig. 1 XPS N 1s results after deconvolution of CTF materials (a) DCP, (b) *p*DCB, (c) DCBP, (d) *p*DCB-400, (e) *p*DCB-600 and (f) *p*DCB-750. Fig. 1b and e are the same material (for an easier comparison at different *T*).

the corresponding Gaussian functions of the deconvoluted signal in the N 1s XPS data. The results are presented in Table 1.

While 3M-CTFs DCP and DCBP are characterized by the highest content of pyridinic nitrogen (52.1% and 48.6%, respectively), 3M-CTF *p*DCB contains the highest content of graphitic N (46.3%) (Table 1, entries 1–3). For the 3T-CTFs based on 1,4-dicyanobenzene (*p*DCB), the highest share of pyridinic nitrogen is observed in *p*DCB-400 and this value decreases at higher temperatures in the second temperature treatment step in accordance with elemental analysis (Table 1, entries 4–6). In general, the share of graphitic nitrogen should increase upon increasing the temperature. It is not clear why the graphitic nitrogen content decreases when increasing the temperature further from 600 to 750 °C. Upon decomposition of an 'ideal' triazine framework structure, graphitic nitrogen (N_{gra}) is expected to be more thermodynamically stable compared to pyridinic nitrogen (N_{pyri}); therefore N_{pyri} should be lost primarily.[36] However, it should be noted that there are two other possible reasons for this deviation. The reaction time for 3T-CTF *p*DCB-400 is much longer (40 hours instead of 10 hours) as otherwise no porous material was obtained. Moreover, extra pure $ZnCl_2$ was used for 3T-CTF *p*DCB-750, therefore only little water is in the system and together with high temperatures this could contribute to the deviation in nitrogen configurations.

There are multiple factors contributing to the electrocatalytic activity in the ORR[3] like the nitrogen content and its configuration and the surface area and porosity of the CTFs as well as the degree of defects or if hierarchical structures are present in the framework. Therefore, further characterization was carried out by Raman spectroscopy in order to gain more insight into the structural properties of CTFs. A more distinct hierarchical structure contributes to a higher number of catalytic active sites and can facilitate active site exposure during the ORR process.[3] The presence of amorphous carbon and defects is indicated by two spectral features at approximately 1350 and 1600 cm^{-1} in the Raman spectra for all CTFs, as displayed in Fig. 2. The two distinct bands can be identified as the characteristic D and G bands of carbon materials.[15,37] The G band (around 1580 cm^{-1}) is related to the stretching of the C–C bonds in graphitic materials and is common to all sp^2-hybridized carbon allotropes.[38] The other band, coined D band, is observed around 1350 cm^{-1} and arises from the presence of atomic-scale disorder or defects in sp^2-hybridized carbon systems.[38] Notably, the corresponding 2D peak at about 2700 cm^{-1}, which originates from a two-phonon process, is very broad and barely visible (see the full Raman spectrum of exemplary 3M-CTF *p*DCB in Fig. S2, ESI†).[37,39] This observation is, however, consistent with the presence of significant defects and amorphous carbon that also affects the electronic structure of the sp^2 carbon, which is relevant for the 2D band. The degree of disorder and defects in amorphous carbon materials is usually quantified by analyzing the relative intensities of the D and G bands (I_D/I_G).[38] The higher the ratio, the higher the disorder in the carbon material[39] and for CTF materials this applies consequently to the defect concentration in the carbonized domains. The observed I_D/I_G ratios for CTFs are reported in Table 1. The comparison of the I_D/I_G ratios of the 3M-CTFs reveals that 3M-CTF DCP has the largest I_D/I_G ratio while DCBP possesses the lowest (Table 1, entries 1–3). A high number of defects in 3M-CTF DCP agrees well with the highest amount of pyridinic nitrogen (N 1s XPS data, Table 1, entries 1–3) content. This indicates a defective structure, since pyridinic nitrogen is located at the edge or defect sites, resulting in a high intensity of the D band.[39] Based on the lowest pyridinic nitrogen ratio in 3M-CTF *p*DCB, the I_D/I_G ratio of 3M-CTF *p*DCB was expected to be the lowest compared to those of the other 3M-CTFs; however, the I_D/I_G ratio of 3M-CTF *p*DCB is higher than that of 3M-CTF DCBP. This might be due to two reasons: (1) the nitrogen content in *p*DCB is larger than that of DCBP (more than double, Table 1, entries 2 and 3),

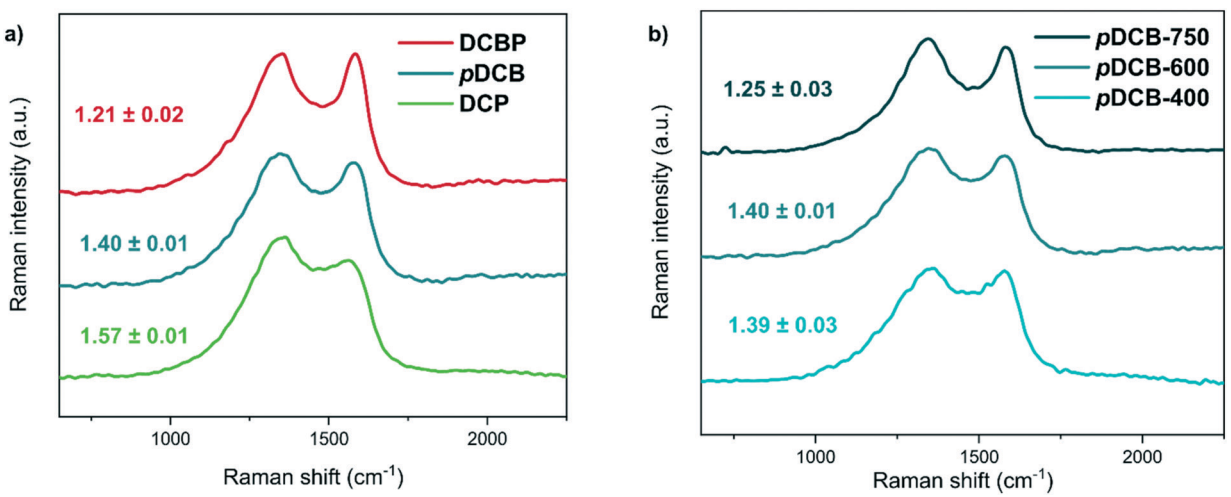

Fig. 2 Raman spectra and corresponding I_D/I_G of the (a) 3M-CTFs and (b) 3T-CTFs materials.

meaning that the total pyridinic N% in *p*DCB is higher, or (2) 3M-CTF *p*DCB may have the larger effect of the valley graphitic N species as the valley graphitic N species are also situated at the edge or defect sites and equally contribute to the increase of the I_D/I_G ratio as pyridinic N.[39] Regarding the 3T-CTFs based on 1,4-dicyanobenzene (*p*DCB), there is almost no change in the I_D/I_G ratios by increasing the temperature from 400 to 600 °C (Table 1, entries 4 and 5). In principle, we would expect to see a decrease in the I_D/I_G ratio for 3T-CTF *p*DCB-600 due to the decrease in pyridinic nitrogen ratio because of further partial carbonization. Indeed, there is an increase in graphitic nitrogen (N 1s XPS, N_{gra} [%] Table 1, entries 4 and 5) and the expected decrease in the I_D/I_G ratio is most likely compensated for by an increase of graphitic N. However, no change in the I_D/I_G ratios between 400 and 600 °C is observed. The significant decrease in the I_D/I_G ratio with further increase of synthesis temperature (from 600 to 750 °C) is probably attributed to the reduced pyridinic nitrogen content. As a result, a lower defect concentration in the structure of the sp^2 carbon systems can be obtained only at higher temperature (>600 °C).

To assess the ORR performance in order to correlate the material structure with the electrochemical activity of synthesized CTF materials, we carried out electrochemical experiments with a rotating disk electrode (RDE) in alkaline media. Since N moieties are protonated in acidic conditions, and this affects the electrochemical response at the aforementioned materials, alkaline media were chosen for the electrochemical studies.[3] The cyclic voltammetry (CV) experiments were carried out at a rotation rate of 2500 rpm in O_2-saturated 0.1 M KOH. Fig. 3a illustrates the ORR activity of the respective 3M-CTF materials including Carbon Super P and 10 wt% Pt/C. Well-formed sigmoidal reduction

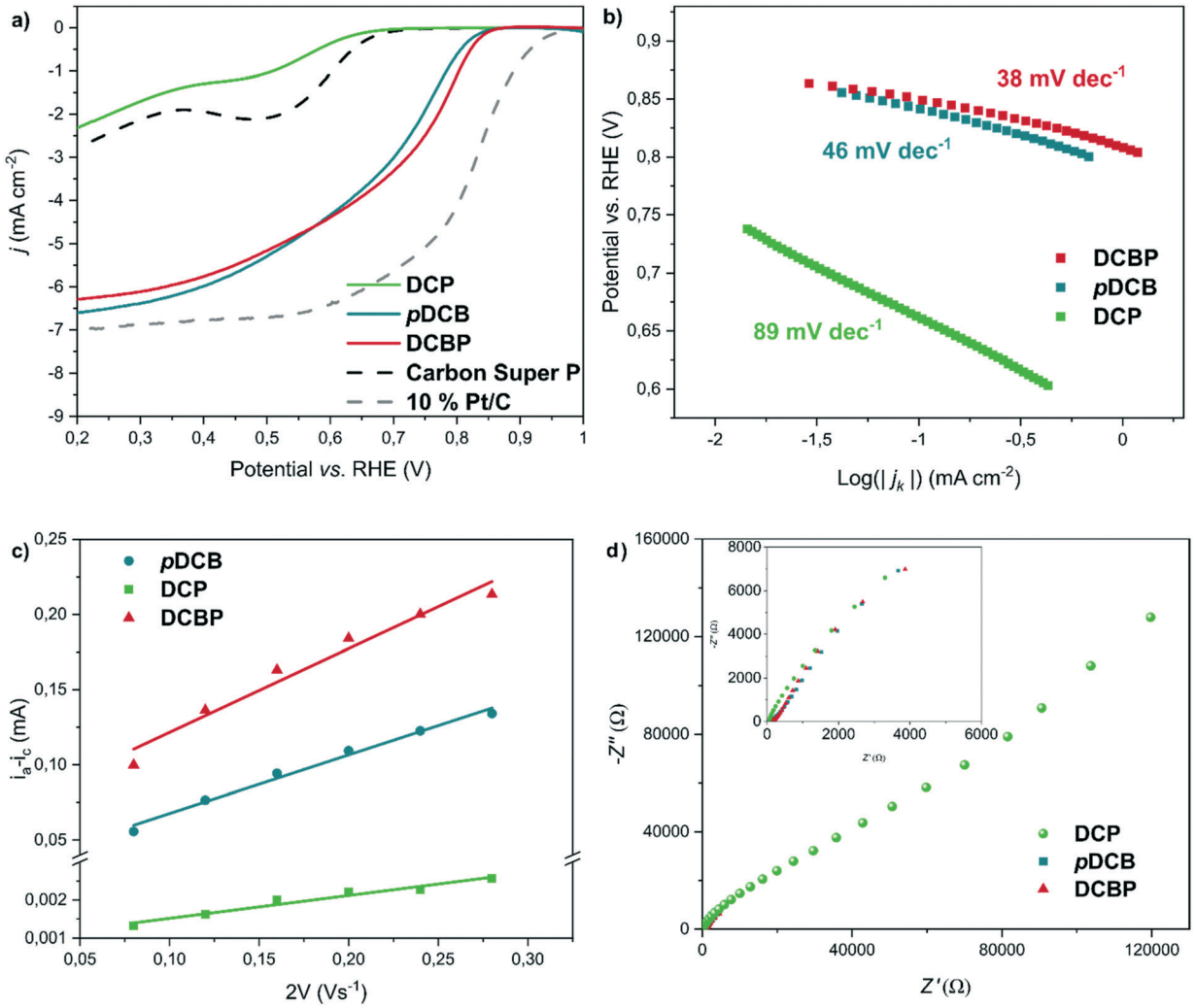

Fig. 3 (a) Voltammograms of the 3M-CTFs on coated glassy carbon RDE including 10 wt% Pt/C and Carbon Super P in O_2-saturated 0.1 M KOH at 10 mV s^{-1} and 2500 rpm. (b) Tafel plots (data taken from the linear regions of the potential *vs.* logj_k at low current densities). (c) Plots for determination of the double layer capacitance based on scan rate-dependent cyclic voltammetry scans in the non-faradaic range (see Fig. S4, ESI,† for CVs used to obtain these plots). (d) Nyquist plots recorded at the OCP and 2500 rpm.

Table 2 Comparison of CTF materials' RDE data collected under the conditions of O_2-saturated 0.1 M KOH at 2500 rpm. Entries 2 and 5 are the same material (again for an easier comparison at different *T*)

Entry	CTF	$E_{-0.1\ mA\ cm^{-2}}$ [V *vs.* RHE]	$E_{1/2}$ [V *vs.* RHE]	$j_{0.2\ V}$ [mA cm^{-2}]	Tafel slope [mV dec^{-1}]	C_{dl} [mF cm^{-2}]
1	DCP	0.66	—	−2.3	89	0.05 ± 0.005
2	*p*DCB	0.84	0.68	−6.6	46	3.10 ± 0.17
3	DCBP	0.85	0.71	−6.3	38	4.43 ± 0.42
4	*p*DCB-400	0.65	—	−2.0	88	0.05 ± 0.002
5	*p*DCB-600	0.84	0.68	−6.6	46	3.10 ± 0.17
6	*p*DCB-750	0.88	0.75	−6.2	56	6.72 ± 0.78
7	DCBP-750	0.90	0.79	−5.1	55	10.6 ± 0.59
8	Carbon super P®	0.69	0.57	−2.8	75	—
9	10 wt% Pt/C	0.96	0.82	−6.9	67	—

waves are obtained with all electrodes, while the limiting current densities and overpotentials are quite different (Table 2, entries 1–3 and 8–9). Amongst the 3M-CTFs, DCBP exhibits the closest onset potential (0.85 V *vs.* RHE) also compared to the benchmark 10 wt% Pt/C with only a 0.11 V larger onset potential. This is most probably due to the smallest amount of total pyridinic nitrogen and the lowest degree of disorder in DCBP (Table 1, entries 1–3). In contrast, *p*DCB shows the highest limiting current density of −6.6 mA cm^{-2}, even slightly smaller than that of the benchmark 10 wt% Pt/C with −6.9 mA cm^{-2} and this might be ascribed to the largest surface area (2358 $m^2\ g^{-1}$) and pore volume (2.18 $cm^3\ g^{-1}$) as well as the high amount of total graphitic nitrogen (Table 1, entries 1–3). Despite having the highest nitrogen content and largest total pyridinic nitrogen sites, the electrochemical performance of DCP is the lowest, even smaller than that of Carbon Super P. Whereas some reports[13,17] suggest that pyridinic nitrogen sites are more active in the ORR, this seems not to be the case here. It seems that the more dominant parameters for the overall ORR performance are the highest degree of disorder (I_D/I_G = 1.57), the smallest surface area (1050 $m^2\ g^{-1}$), the pore volume (0.57 $cm^3\ g^{-1}$) and the micro-porosity. In contrast to the LSV of DCBP and *p*DCB (Fig. 3a), the LSV curve of DCP shows a plateau in the potential range of 0.4 to 0.5 V *vs.* RHE similar to that of Carbon Super P, indicating a $2e^-$ reduction process of O_2 to hydrogen peroxide (HO_2^-) formation followed by further reduction to hydroxyl ions (OH^-) at higher overpotentials.[11,40] On the other hand, the ORR seems to follow the direct $4e^-$ reduction for both DCBP and *p*DCB, similar to Pt/C based on the first glance of their LSV results (Fig. 3a). However, these outcomes have to be supported by further analysis.

For the 3M-CTFs, Tafel plots and their slopes are presented in Fig. 3b to compare the electron transfer kinetics at the electrolyte–catalyst interface. The plots show linear regions at low current densities, and based on Tafel slopes, DCBP and *p*DCB show relatively small but similar slopes (38 and 46 mV dec^{-1}, respectively) close to the slope of Pt/C (67 mV dec^{-1}, not shown in the figure). In contrast, the slope for DCP is significantly steeper (89 mV dec^{-1}), indicating a large kinetic limitation for the ORR at the DCP–electrolyte interface despite the large pyridinic nitrogen content. The determination of the double layer capacitance (C_{dl}) of the CTFs is important as it is proportional to the actual electrochemically active surface area (ECSA) where the charge transfer takes place. The CV scans at varying scan rates in the non-faradaic potential region were thus obtained for the 3M-CTFs (Fig. S4, ESI†) and used to obtain the double layer capacitance (Fig. 3c and Table 2 (entries 1–3)). The lowest C_{dl} value of DCP (0.05 mF cm^{-2}) is in good correlation with the lowest specific surface area and pore volume as well as poor ORR activity. On the other hand, the highest C_{dl} value (4.43 mF cm^{-2}) is observed at DCBP, implying that the highest ECSA correlates with its more positive onset potential and half-wave potential (Table 2, entry 3). Despite the lower total nitrogen content and smaller specific surface area of DCBP compared to *p*DCB, the smaller degree of disorder accompanied by the larger ECSA results in a better charge transfer at the DCBP–electrolyte interface. The observed smaller limiting current density of DCBP in the diffusion-controlled region (~0.2 V *vs.* RHE) compared to *p*DCB is most probably due to its smaller surface area, the pore volume and total graphitic N sites (Fig. 3a and Table 1 (entries 2 and 3)). The larger pore volume of *p*DCB could increase the mass transport efficiency and surpass the lower ECSA effect.

To do further electrochemical characterization of the CTFs, electrochemical impedance spectroscopy was applied. As the main interest is to obtain and compare the pure charge transfer resistances (R_{ct}) of the CTF materials in the kinetic region, the measurements were carried out at the open circuit potential (OCP ~0.91 V *vs.* RHE). In this region, the total current over the electrochemical cell is zero and the impact of mass-transport resistance is close to zero, too. Otherwise, the physicochemical processes at the electrode/electrolyte interface are a mixture of mass transfer and charge transfer (kinetic transfer) processes at smaller potentials (*vs.* RHE) and it can happen that it becomes dominated by mass transfer for potentials far away from the kinetic region. In this case, the impedance spectra could be hard to interpret due to superimposed features of different effects as the Warburg diffusion element (*W*) which is a 45° linear region will appear at the high-frequency region.[41]

Nyquist plots of the 3M-CTFs are presented in Fig. 3d and indicate that a charge transfer resistance (R_{ct}) for DCP may be smaller when compared to that of the other two 3M-CTFs. In particular, at high frequencies, this can be clearly seen as the slope of the Warburg diffusion line becomes steeper. However, this data pattern can only be confirmed when fitting the experimental EIS data to the specific equivalent circuit that suits the interface process. If a smaller R_{ct} value was obtained for DCP, this means that the interface reactions are controlled by mass and charge transfer processes. However, the interface process is dominated by mass transfer rather than charge transfer. To extract the R_{ct} values for the EIS spectra of DCP, *p*DCB and DCBP, using NOVA 1.1 software, the EIS spectra were fitted to the suggested equivalent circuit models as shown in Fig. S8A and B (ESI†), respectively. Interestingly, the proposed equivalent circuit model in Fig. S8A† gave well-fitted data for the Nyquist and Bode plots of DCP (Fig. S9a and b, ESI†) with a goodness of fit (x^2) of 0.432. Also, the same equivalent circuit was used to convergently fit the EIS spectra of *p*DCB (Fig. S9c and d, ESI†) with the x^2 obtained as 3.097. In contrast, the equivalent circuit in Fig. S8B† was employed to convergently fit the EIS spectra of DCBP with x^2 obtained as 2.73. However, the fitted data for DCBP does not fit well with the experimental data of the Nyquist and Bode plots (Fig. S9e and f, ESI†), in particular at medium- and lower-frequency regions. This dictates that data of the real electrochemical system for the DCBP thin-film catalyst may follow a more complex equivalent circuit. As shown in Table S4 (ESI†), the obtained R_{ct} value for DCP of 48.75 Ω is lower than the values

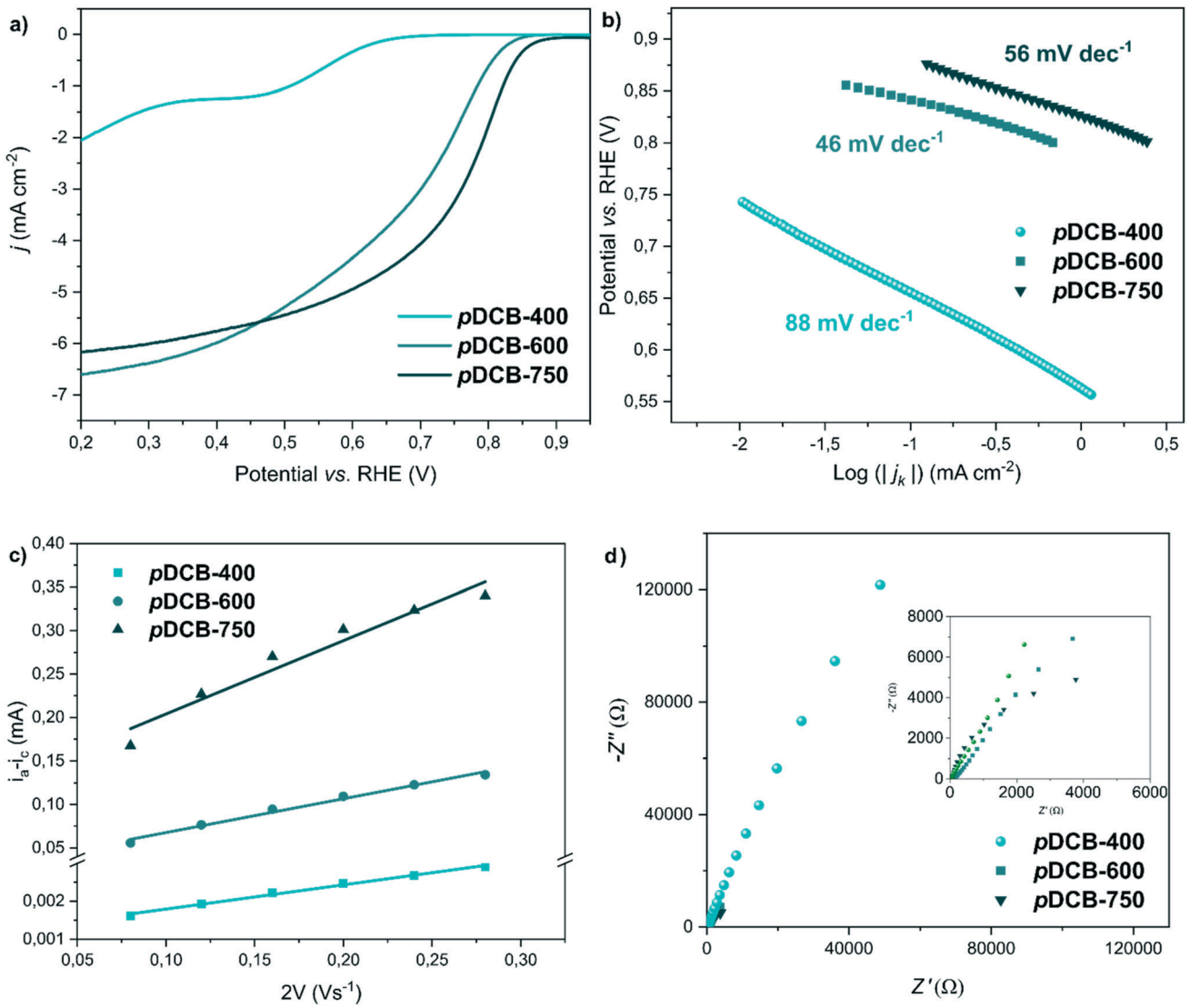

Fig. 4 (a) Voltammograms of the 3T-CTFs based on *p*DCB monomer coated on glassy carbon RDE in O_2-saturated 0.1 M KOH at 10 mV s^{-1} and 2500 rpm. (b) Tafel plots (data taken from the linear regions of the potential *vs.* log j_k at low current densities). (c) Plots for determination of the double layer capacitance based on scan rate-dependent cyclic voltammetry scans in the non-faradaic range (see Fig. S5, ESI,† for CVs used to obtain these plots). (d) Nyquist plots recorded at the OCP and 2500 rpm.

for *p*DCB and DCBP (270.18 Ω and 165.73 Ω, respectively). This signifies a stronger effect of the mass transfer process that governs interface reactions at DCP compared to mass transfer processes at both DCBP and *p*DCB.

Besides the electrochemical characterization for the 3M-CTFs, the electrochemical activities of 3T-CTFs synthesized from 1,4-dicyanobenzene (*p*DCB) were also tested. Fig. 4a presents well-formed sigmoidal oxygen reduction waves for all 3T-CTFs obviously with different onset potentials and current densities (Table 2, entries 4–6). *p*DCB-400 with the highest nitrogen content (also with the largest pyridinic nitrogen ratio) and a relatively small surface area and pore volume possesses the lowest ORR activity compared to the other two samples (Table 2, entries 4–6). The voltammogram of *p*DCB-400 shows a plateau, similar to 3M-CTF DCP, between 0.4 and 0.55 V *vs.* RHE, indicating that the oxygen reduction probably occurs predominantly as a $2e^-$ reduction process. As shown in Fig. 4a, the ORR activity is greatly enhanced and the oxygen reduction pathway is likely changed from $2e^-$ to $4e^-$ by raising the temperature from 400 to 600 °C in the second step of the ionothermal synthesis despite just a small change in the nitrogen contents and almost the same I_D/I_G ratios of *p*DCB-400 and *p*DCB-600 (Table 1, entries 4 and 5). This distinct activity increase is likely associated with the increase of graphitic nitrogen (Table 1, entries 4 and 5), resulting in improved electrical conductivity. In addition, the larger surface area (more than double), the larger pore volume (more than threefold), and the transition from a microporous to a mesoporous structure (Fig. S1b, ESI†) are essential parameters for the exposure of active N-sites and efficient charge and mass transfer. CTF *p*DCB-750 possesses the most positive onset and half-wave potentials amongst the 3T-CTFs (even more positive than that of previously discussed 3M-CTF DCBP) (Table 2, entries 3–6). This is again as previously discussed most likely due to the smallest portion of defects (the most hierarchical structure) and the smallest amount of total pyridinic N that *p*DCB-750 possesses. On the other hand, the current density of *p*DCB-600 (−6.6 mA cm^{-2}) is slightly higher than that of *p*DCB-750 (−6.2 mA cm^{-2}). This is attributed to higher nitrogen content and the largest amount of graphitic N-sites of *p*DCB-600, while the surface area and pore volume of *p*DCB-600 are slightly smaller (Table 1, entries 5 and 6).

Tafel plots and the respective slopes of 3T-CTFs are presented in Fig. 4b showing that *p*DCB-400 (similar to DCP) exhibits the largest kinetic limitation for the ORR in accordance with the presented analyses. The Tafel slope for *p*DCB-750 is, however, larger than for *p*DCB-600, whereas it shows more positive onset and half-wave potentials. This might be explained by the lower current density that *p*DCB-750 possesses and by a smaller N-content and total number of graphitic N sites. Besides an increase in the degree of graphitization with increasing temperature, the smaller amount of total graphitic N results in a relatively larger kinetic limitation for the ORR at *p*DCB-750. The double layer capacitance plots of these CTFs, obtained using the CV scans with varying scan rates again in the non-faradaic potential region (Fig. S5, ESI†), are shown in Fig. 4c and their corresponding C_{dl} values are reported in Table 2 (entries 4–6). The smallest C_{dl} value of 0.05 mF cm^{-2} is observed at *p*DCB-400 (again similar to DCP), and thus showing the lowest ECSA value amongst the aforementioned CTFs, in accordance with its lowest specific surface area (1172 $m^2\ g^{-1}$), pore volume (0.66 $cm^3\ g^{-1}$) and poor ORR kinetics. In contrast, the largest C_{dl} value of 6.72 mF cm^{-2} is observed at *p*DCB-750 (more than double that of *p*DCB-600 with 3.10 mF cm^{-2}), indicating the highest ECSA and therefore showing the most positive onset potential. Indeed, it was not surprising to obtain the most positive onset potential at *p*DCB-750 due to its largest pore volume of 2.49 $cm^3\ g^{-1}$ as higher porosity causes higher exposure of active N-sites, resulting in better ORR kinetics.[4] These C_{dl} values are in a good agreement with the CTFs' corresponding specific surface areas and pore volumes, which are increased with rising synthesis temperatures. Electrochemical impedance spectroscopy measurements were carried out to compare the charge transfer resistances of the 3T-CTFs, and their corresponding Nyquist plots are illustrated in Fig. 4d. The Nyquist plot of *p*DCB-400 is relatively steep compared to the others, stressing its low conductivity, while *p*DCB-750 shows a plot converging to a half-circular shape, as seen in the inset in Fig. 4d. There is an obvious increase in the electrical conductivity along with the temperature increase, and this is in accordance with the previous study[26] (see inset in Fig. 4d). To extract R_{ct} values for each EIS spectrum in Fig. 4d, a suggested equivalent circuit model, as shown in Fig. S8A (ESI†), was also used to convergently fit the EIS spectra of *p*DCB-400, *p*DCB-600 and *p*DCB-750, respectively. Interestingly, the proposed equivalent circuit model to convergently fit the EIS spectra of 3T-CTF *p*DCB (400–750 °C) thin-film catalyst is similar to the proposed equivalent circuit to fit the EIS spectrum of DCP. Based upon the equivalent circuit, the physicochemical processes of the ORR at *p*DCB-400, *p*DCB-600 and *p*DCB-750 thin-film catalysts were controlled by mass-transfer and charge-transfer processes. The R_{ct} values, error values and x^2 from the fitted data can be seen in Table S4 (ESI†). Following the obtained R_{ct} values, *p*DCB-750 offered better anisotropic conductivity for mass-transfer and charge-transfer processes at the electrode/electrolyte interface compared to *p*DCB-400 and pDCB-600. This agrees with our previous statement which showed an increased electrical conductivity of CTF catalysts with rising synthesis temperature.

Since the highest ORR performance was found for DCBP amongst all the tested CTFs, while *p*DCB-750 revealed the most positive onset and half-wave potentials, we did further optimization of the electrocatalytic performance. Therefore, DCBP-750 was synthesized from the biphenylic monomer 4,4′-biphenyldicarbonitrile, again *via* an ionothermal route, where the synthesis temperature was raised to 750 °C in the second step. Like the other CTFs, elemental analysis and nitrogen-physisorption measurements regarding the N

content and structural parameters, respectively, were also carried out and are reported in Table 1 (entry 7). DCBP-750 shows a type IV isotherm with an H2 hysteresis loop (between 0.4 and 0.8 p/p_0), corresponding to a mesoporous structure (Fig. S1c, ESI†). The nitrogen content decreases significantly compared to the aforementioned material synthesized *via* the standard ionothermal route with only 600 °C synthesis temperature in the second step. As expected, the N content decreases further upon increasing the synthesis temperature from 600 to 750 °C for DCBP-750 and the material even contains less nitrogen compared to *p*DCB-750 (Table 1, entries 6 and 7). In contrast to *p*DCB-750, the specific surface area and total pore volume of DCBP-750 do not increase with rising synthesis temperature. Whereas the V_p values of DCBP-750 and DCBP are almost the same, the surface area decreased for enhanced synthesis temperature. The XPS N 1s data of DCBP-750 (Fig. S3a, ESI†) were analyzed to define the ratios of different N species, reported in Table 1 (entry 7). The transition from pyridinic to graphitic N is obvious by increasing the synthesis temperature from 600 to 750 °C, implying the improved conductivity of DCBP-750 compared to DCBP. Alongside its higher conductivity, Raman spectroscopy (Fig. 3Sb, ESI†) reveals that DCBP-750 also possesses the smallest number of defects (I_D/I_G = 1.19) amongst all the CTF materials, suggesting a superior framework structure (Table 1, entries 1–7).

The ORR performance of DCBP-750 was also tested and compared to that of *p*DCB-750 under similar conditions. As shown in Fig. 5a and reported in Table 2 (entries 6 and 7), both samples show sigmoidal waves with different onset potentials and current densities. The onset potential of DCBP-750 (0.90 V *vs.* RHE) is further shifted to the more positive region compared to *p*DCB-750 and it is only 0.06 V larger than that of the benchmark 10 wt% Pt/C. This improved onset potential is most likely associated to the smallest degree of disorder and total pyridinic N that DCBP-750 possesses amongst all CTFs studied in this work (Table 1). In spite of the improved onset and half-wave potentials of DCBP-750, the limiting current density (−5.1 mA cm^{-2}) is smaller than for *p*DCB-750 (−6.2 mA cm^{-2}) and it is further decreased compared to DCBP (−6.3 mA cm^{-2}) when prepared at elevated synthesis temperature. This difference could be first attributed to the smaller surface area and pore volume of DCBP-750 (Table 1, entries 3, 6 and 7). However, the double layer capacitance (Fig. S7a, ESI,† and Table 2 (entries 3 and 7)) is further increased from 4.43 to 10.6 mF cm^{-2} by increasing temperature, indicating an increase in ECSA. Therefore, the reason behind the limiting current density decrease is most likely the smallest total graphitic N content and the accessible active sites for binding and activation of O_2, (Table 1, entries 3, 6 and 7). The smallest amount of total graphitic N might limit the overall ORR performance despite the improved charge transfer.

Comparing the Tafel slopes of the materials shows that the slope for DCBP-750 (Fig. S7b, ESI†) is higher than for DCBP (55 and 38 mV dec^{-1}, respectively), suggesting larger kinetic limitation, and this is in a good agreement with its smaller diffusion-limiting current density. The increase in the Tafel slope might be explained with a decrease in total graphitic N active sites by raising the synthesis temperature. Finally, the charge transfer resistances were also tested and the corresponding Nyquist plots of both DCBP-750 and *p*DCB-750 are shown in Fig. 5b. A large difference in their EIS responses can clearly be seen and interestingly, based on the proposed equivalent circuit model (Fig. S8C, ESI†), the electrocatalytic reaction at the electrode/electrolyte interface for DCBP-750 was only governed by the kinetic transfer process, also known as charge transfer process, with an R_{ct} value of 2253 Ω. This can be described by a semicircle-shaped Nyquist plot without the involvement of the Warburg

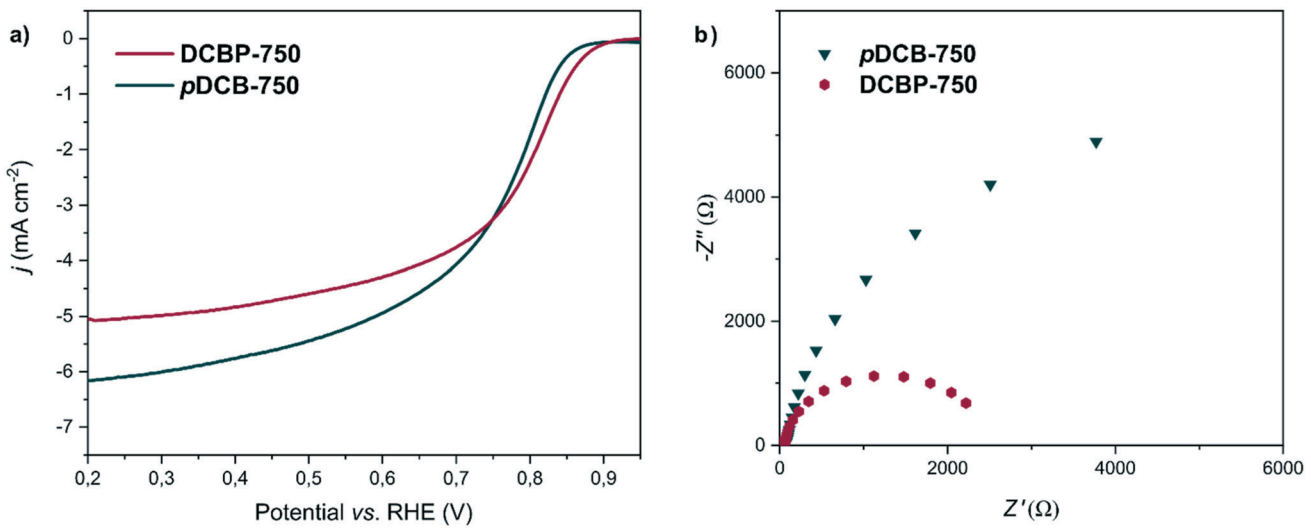

Fig. 5 (a) Voltammograms of DCBP-750 and *p*DCB-750 on coated glassy carbon RDE in O_2-saturated 0.1 M KOH at 10 mV s^{-1} and 2500 rpm. (b) Nyquist plots recorded at the OCP and 2500 rpm.

diffusion line in Fig. 5b, implying that DCBP-750 provides better anisotropic conductivity than *p*DCB-750 through the larger electroactive surface area. For that reason, this gave more catalytic sites for molecular O_2 to be adsorbed within DCBP-750 thin-film catalyst to undergo a further reduction reaction process. In addition, well-fitted Nyquist and Bode plots without the constant phase element (CPE) were obtained, indicating a homogenous catalytic surface for DCBP-750, thus providing better electrode kinetics for the adsorbed molecular O_2. Therefore, the interface reaction is dominated only by the kinetic transfer process. Additionally, based upon the Bode plots of *p*DCB-750 and DCBP-750 (Fig. S11b and d, ESI†), when comparing the phase angle (θ) for both materials, there is a decrease in the θ value of DCBP-750. The θ values for *p*DCB-750 and DCBP-750 were found to be 75.28 and 68.80, respectively. This supports a faster kinetic transfer process at DCBP-750 compared to *p*DCB-750. This data trend is in agreement with the proposed equivalent circuits (Fig. S8a and c†) that fitted well to experimental EIS data of *p*DCB-750 and DCBP-750 (Fig. S11a–d, ESI†). In addition, the high anisotropic conductivity of DCBP-750 comes from the transition of pyridinic to graphitic N (as previously discussed with XPS N 1s data) accompanied by the smallest degree of disorder upon raising the synthesis temperature (Table 1, entries 3 and 7). Therefore, the impedance data are well in agreement with the obtained more positive onset and half-wave potentials of DCBP-750, proving its fast ORR kinetics amongst all the CTFs studied in this work. In contrast, based on the equivalent circuit for *p*DCB-750 (Fig. S8A, ESI†), a Warburg diffusion element (W) was included in the equivalent circuit to convergently fit the EIS data. Therefore, electrocatalytic reactions at the interface are controlled by mass transfer and charge transfer processes. However, based on the fitted data, the R_{ct} value for *p*DCB-750 was obtained to be 41.5 Ω, which is lower than the R_{ct} value of DCBP-750. This data trend has been expected as lower R_{ct} may be due to a strong influence by the mass-transfer process.[41] Thus, it can be concluded that the electrocatalytic reactions at *p*DCB-750 are dominated by mass transfer rather than the kinetic transfer process. This can be clearly seen in Fig. S12 (ESI†), an enlargement of the EIS spectrum from *p*DCB-750, where a 45° straight line at the high-frequency region is clearly observed. However, we think that both R_{ct} values cannot be compared quantitatively, as the interface processes, analysed from the equivalent circuit models at both materials, are different. Overall, the ORR performance of DCBP-750 is comparable to that of the benchmark 10 wt% Pt/C and other state-of-the-art metal-free carbon-based electrocatalysts in terms of onset potential, half-wave potential and limiting current density (Table S5, ESI†).

In addition to high ORR performance of the CTF materials, long term electrocatalytic stability of metal-free CTF materials is a crucial aspect for the practical applications in ORR. Therefore, a stability test of the best performing CTF DCBP-750 was carried out and the chronoamperometric response of DCBP-750 at a constant potential of 0.65 V *vs.* RHE is shown in Fig. 6. The current density decreases slightly faster during the first hour of measurement, however, it stabilized after 6 hours, and retained 80% of the initial current density, which confirms very good stability of the best performing metal-free CTF DCBP-750 over a long period of time.

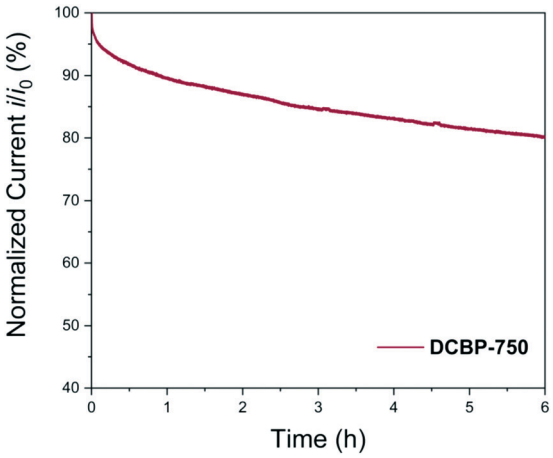

Fig. 6 Chronoamperometric response of DCBP-750 in O_2-saturated 0.1 M KOH at 0.65 V *vs.* RHE and 1600 rpm.

Conclusions

Metal-free CTF materials have been successfully synthesized based on different monomer units and different synthesis temperatures *via* an ionothermal route and were tested for the ORR in alkaline media. Due to the highest hierarchical mesoporous structure and therefore largest ECSA, the most positive onset and half-wave potentials are obtained for DCBP compared to the other 3M-CTFs. The obtained highest $j_{0.2V}$ of *p*DCB (slightly smaller than that of the benchmark 10 wt% Pt/C) corresponds to the larger specific surface area, total pore volume and the highest graphitic N content. The comparison of 3T-CTFs based on the monomer 1,4-dicyanobenzene (*p*DCB) reveals that the ORR performance is greatly increased with rising temperature, influenced by an obvious transition from pyridinic to graphitic N, increase in conductivity, specific surface area, and pore volume and a more hierarchical structure opposed by a decrease in N content. Although the most positive onset potential is obtained at 750 °C, the current density is slightly decreased when raising the temperature from 600 to 750 °C. This is due to the decrease in the number of graphitic N active sites, which limits the maximum achievable limiting current density. While higher conductivity and a low degree of disorder, responsible for the shift of onset potential towards more positive potentials, are achievable along with elevated temperature, the decrease in the content of graphitic N, responsible for binding and activating O_2, is more essential for the overall ORR performance. Therefore, the trade-off point is important for obtaining an optimal activity. As a result of further electrocatalytic optimization *via* monomer and synthesis temperature variations, the most positive onset

potential (0.9 V *vs.* RHE) is achieved for DCBP-750, being only 0.06 V higher than that of the benchmark 10 wt% Pt/C. However, the limiting current density of DCBP-750 is below that of the other most active CTFs (*p*DCB-750 and DCBP), also showing the trade-off between an improved electrical conductivity, the highest ECSA and total graphitic N content. The ORR pathways at CTFs were compared to those of Carbon Super P and 10 wt% Pt/C (showing $2e^-$ and $4e^-$, respectively). Based at first glance on their voltammograms, it seems that O_2 is likely reduced *via* $2e^-$ at DCP while it is $4e^-$ at the other CTFs depending on the applied monomers. In addition, the transition from $2e^-$ to $4e^-$ oxygen reduction is most probable by raising the synthesis temperature. However, these results about the mechanistic pathways have to be supported by further analysis, which is the subject of our next study. The findings and observations in this study may shed light on the rational catalyst design for energy storage and conversion devices.

Conflicts of interest

There are no conflicts to declare.

Acknowledgements

This study was supported by the Deutsche Forschungsgemeinschaft (DFG, German Research Foundation) under Germany's Excellence Strategy within the Exzellenzcluster 2186 "The Fuel Science Center" ID: 390919832. TS acknowledges the receipt of a postdoctoral fellowship from The Scientific and Technological Research Council of Turkey (TÜBİTAK), Republic of Turkey.

Notes and references

1 J. Liu, Y. Hu and J. Cao, *Catal. Commun.*, 2015, **66**, 91–94.
2 L. Tong, Z. Shao, Y. Qian and W. Li, *J. Mater. Chem. A*, 2017, **5**, 3832–3838.
3 Y. Cao, Y. Zhu, X. Chen, B. S. Abraha, W. Peng, Y. Li, G. Zhang, F. Zhang and X. Fan, *Catal. Sci. Technol.*, 2019, **9**, 6606–6612.
4 D. S. Yang, S. Chaudhari, K. P. Rajesh and J. S. Yu, *ChemCatChem*, 2014, **6**, 1236–1244.
5 K. A. Stoerzinger, M. Risch, B. Han and Y. Shao-Horn, *ACS Catal.*, 2015, **5**, 6021–6031.
6 G. Wu, K. L. More, C. M. Johnston and P. Zelenay, *Science*, 2011, **332**, 443–447.
7 L. Lin, Q. Zhu and A.-W. Xu, *J. Am. Chem. Soc.*, 2014, **136**, 11027–11033.
8 V. Celorrio, L. Calvillo, C. A. van den Bosch, G. Granozzi, A. Aguadero, A. E. Russell and D. J. Fermín, *ChemElectroChem*, 2018, **5**, 3044–3051.
9 V. Celorrio, L. Calvillo, E. Dann, G. Granozzi, A. Aguadero, D. Kramer, A. E. Russell and D. J. Fermín, *Catal. Sci. Technol.*, 2016, **6**, 7231–7238.
10 V. Celorrio, L. Calvillo, G. Granozzi, A. Russell and D. Fermin, *Top. Catal.*, 2018, **61**, 154–161.
11 T. Sönmez, S. J. Thompson, S. W. Price, D. Pletcher and A. E. Russell, *J. Electrochem. Soc.*, 2016, **163**, H884–H890.
12 D. Pletcher, X. Li, S. W. Price, A. E. Russell, T. Sönmez and S. J. Thompson, *Electrochim. Acta*, 2016, **188**, 286–293.
13 J. Chen, X. Wang, X. Cui, G. Yang and W. Zheng, *Chem. Commun.*, 2014, **50**, 557–559.
14 T. Xing, Y. Zheng, L. H. Li, B. C. Cowie, D. Gunzelmann, S. Z. Qiao, S. Huang and Y. Chen, *ACS Nano*, 2014, **8**, 6856–6862.
15 D. Deng, X. Pan, L. Yu, Y. Cui, Y. Jiang, J. Qi, W.-X. Li, Q. Fu, X. Ma and Q. Xue, *Chem. Mater.*, 2011, **23**, 1188–1193.
16 H. Yu, L. Shang, T. Bian, R. Shi, G. I. Waterhouse, Y. Zhao, C. Zhou, L. Z. Wu, C. H. Tung and T. Zhang, *Adv. Mater.*, 2016, **28**, 5080–5086.
17 C. V. Rao, C. R. Cabrera and Y. Ishikawa, *J. Phys. Chem. Lett.*, 2010, **1**, 2622–2627.
18 J. Artz, *ChemCatChem*, 2018, **10**, 1753–1771.
19 P. Kuhn, M. Antonietti and A. Thomas, *Angew. Chem., Int. Ed.*, 2008, **47**, 3450–3453.
20 A. P. Cote, A. I. Benin, N. W. Ockwig, M. O'Keeffe, A. J. Matzger and O. M. Yaghi, *Science*, 2005, **310**, 1166–1170.
21 C. S. Diercks and O. M. Yaghi, *Science*, 2017, **355**, eaal1585.
22 P. Kuhn, A. Forget, D. Su, A. Thomas and M. Antonietti, *J. Am. Chem. Soc.*, 2008, **130**, 13333–13337.
23 A. Bhunia, V. Vasylyeva and C. Janiak, *Chem. Commun.*, 2013, **49**, 3961–3963.
24 P. Puthiaraj, Y.-R. Lee, S. Zhang and W.-S. Ahn, *J. Mater. Chem. A*, 2016, **4**, 16288–16311.
25 G. Wu, D. Li, C. Dai, D. Wang and N. Li, *Langmuir*, 2008, **24**, 3566–3575.
26 L. Hao, S. Zhang, R. Liu, J. Ning, G. Zhang and L. Zhi, *Adv. Mater.*, 2015, **27**, 3190–3195.
27 J. Artz, I. Delidovich, M. Pilaski, J. Niemeier, B. M. Kübber, K. Rahimi and R. Palkovits, *RSC Adv.*, 2018, **8**, 22392–22401.
28 J. Artz, S. Mallmann and R. Palkovits, *ChemSusChem*, 2015, **8**, 672–679.
29 P. Kuhn, A. Thomas and M. Antonietti, *Macromolecules*, 2008, **42**, 319–326.
30 J. Artz and R. Palkovits, *ChemSusChem*, 2015, **8**, 3832–3838.
31 D. Y. Osadchii, A. I. Olivos-Suarez, A. V. Bavykina and J. Gascon, *Langmuir*, 2017, **33**, 14278–14285.
32 G. Tuci, M. Pilaski, H. Ba, A. Rossin, L. Luconi, S. Caporali, C. Pham-Huu, R. Palkovits and G. Giambastiani, *Adv. Funct. Mater.*, 2017, **27**, 1605672.
33 X. Cui, S. Yang, X. Yan, J. Leng, S. Shuang, P. M. Ajayan and Z. Zhang, *Adv. Funct. Mater.*, 2016, **26**, 5708–5717.
34 B. Zheng, J. Wang, F.-B. Wang and X.-H. Xia, *Electrochem. Commun.*, 2013, **28**, 24–26.
35 H. Niwa, K. Horiba, Y. Harada, M. Oshima, T. Ikeda, K. Terakura, J.-i. Ozaki and S. Miyata, *J. Power Sources*, 2009, **187**, 93–97.
36 X. Ning, Y. Li, J. Ming, Q. Wang, H. Wang, Y. Cao, F. Peng, Y. Yang and H. Yu, *Chem. Sci.*, 2019, **10**, 1589–1596.
37 L. Malard, M. Pimenta, G. Dresselhaus and M. Dresselhaus, *Phys. Rep.*, 2009, **473**, 51–87.

38 M. S. Dresselhaus, A. Jorio, M. Hofmann, G. Dresselhaus and R. Saito, *Nano Lett.*, 2010, **10**, 751–758.
39 N. Daems, X. Sheng, I. F. Vankelecom and P. P. Pescarmona, *J. Mater. Chem. A*, 2014, **2**, 4085–4110.
40 J. Masa, A. Zhao, W. Xia, M. Muhler and W. Schuhmann, *Electrochim. Acta*, 2014, **128**, 271–278.
41 R. K. Singh, R. Devivaraprasad, T. Kar, A. Chakraborty and M. Neergat, *J. Electrochem. Soc.*, 2015, **162**, F489–F498.